# Crepuscular Rays for Tumor Accessibility Planning

Rostislav Khlebnikov, Bernhard Kainz, Judith Muehl, and Dieter Schmalstieg, *Member, IEEE*

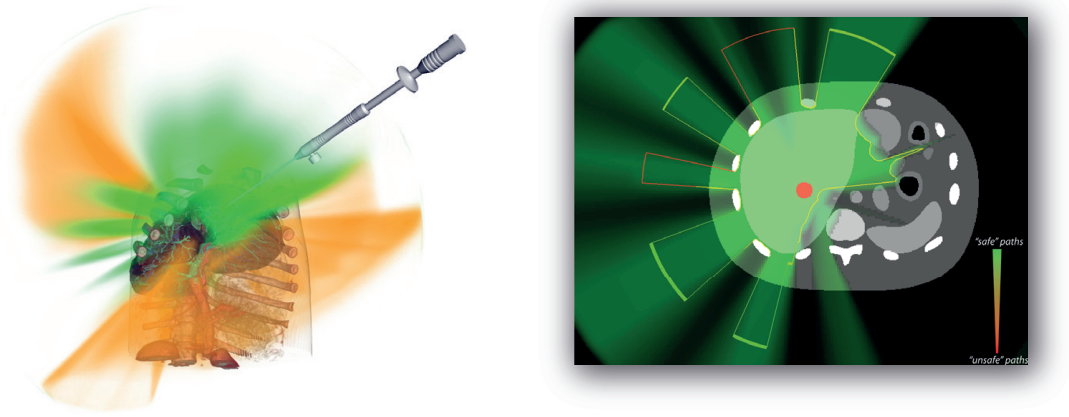


(a) (b)

Fig. 1. Regarding a tumor as a volumetric light source, we estimate the safety of *all* straight access paths in the region of interest based on the light intensity reaching every point. We display the safety information in 3D using direct volume rendering (a) and in 2D slice views that allow millimeter-accurate intervention planning, which are widespread in medicine (b). The 3D view (a) shows the safe (green) and the medium-safe paths (yellow). The 2D slice view (b), shows only the safe paths from the volumetric representation and provides additional information about the extent of safe areas using color-coded thick lines. Thin red lines signify that the available leeway is very small and that the physician must be very precise to use such access areas. In contrast, thick green lines mean that less precision is required, as the corresponding safe area is large. The datasets used in these examples are (a) porcine abdomen CT and (b) artificial XCat patient model [20].

**Abstract**—In modern clinical practice, planning access paths to volumetric target structures remains one of the most important and most complex tasks, and a physician's insufficient experience in this can lead to severe complications or even the death of the patient. In this paper, we present a method for safety evaluation and the visualization of access paths to assist physicians during preoperative planning. As a metaphor for our method, we employ a well-known, and thus intuitively perceivable, natural phenomenon that is usually called *crepuscular rays*. Using this metaphor, we propose several ways to compute the safety of paths from the region of interest to *all* tumor voxels and show how this information can be visualized in real-time using a multi-volume rendering system. Furthermore, we show how to estimate the extent of connected safe areas to improve common medical 2D multi-planar reconstruction (MPR) views. We evaluate our method by means of expert interviews, an online survey, and a retrospective evaluation of 19 real abdominal radio-frequency ablation (RFA) interventions, with expert decisions serving as a gold standard. The evaluation results show clear evidence that our method can be successfully applied in clinical practice without introducing substantial overhead work for the acting personnel. Finally, we show that our method is not limited to medical applications and that it can also be useful in other fields.

**Index Terms**—Accessibility, ray casting, medical visualization.

## 1 Introduction

Planning an optimal access path to harmful structures, such as tumors, within the human body is essential in many medical procedures. In modern clinical practice, the treating physician makes a decision about the trajectories of medical tools or the areas of resection for a particular patient. This decision is usually based solely on the physician's experience with similar interventions and general knowledge of the vulnerable anatomical structures within the human body. This empirical approach leads to a strong dependence of the treatment result on the experience of the clinician. Hildebrand *et al.* [18] have shown that operator experience has a *significant* influence on the treatment outcome of minimally invasive radio frequency ablations of malignant liver tumors. Mueller *et al.* [24] and McDonald *et al.* [22] showed similar effects for coronary interventions and spine surgery. Hence, in certain cases, this unsupervised access-path planning approach may be harmful or even *deadly* for the patient. Even when a navigation system is used for guidance during an intervention (e.g., in neurosurgery), the access path is still chosen empirically by the performing physician in advance, and thus the treatment outcome depends on the physician's experience.

Trajectory planning is a very complex procedure because of the huge amount of available data that must be taken into account. These data are produced using modern imaging modalities such as computed tomography (CT), magnetic resonance imaging (MRI) and its derivatives such as diffusion-tensor imaging (DTI), and many others. Furthermore new imaging modalities (e.g., dual-energy CT) are still being developed, and thus the information load on the physician planning the operation will continue to increase. Therefore, it is crucial to create systems that can integrate these data sources and assist the physician in choosing the access path. A fully automatic determination of the

• *Authors are with Graz University of Technology, E-mail: khlebnikov|kainz|muehl|schmalstieg@icg.tugraz.at.*

*Manuscript received 31 March 2011; accepted 1 August 2011; posted online 23 October 2011; mailed on 14 October 2011.*
*For information on obtaining reprints of this article, please send email to: tvcg@computer.org.*

*best* access path is certainly desirable, but it is currently not possible in every case because of the enormous number of degrees of freedom. For this reason, we propose using visualization to assist the physician's decision-making. This visualization must be able to display all of the available medical data simultaneously to let the physician concentrate on the planning itself. Furthermore, it is beneficial to visualize information about the accessibility of the target structure along with the medical data. However, this visualization should only provide auxiliary information to the physician, leaving the final decision to the human operator.

In this work, we propose a novel multi-stage tumor-accessibility visualization approach that makes it possible to evaluate the safety of *all* possible straight access paths and to display this information in an intuitive way, thus allowing the performing physician to make a more informed decision without limiting treatment options. The intuitiveness of our visualization originates from a basic metaphor: we think of a tumor as an omni-directional volumetric light source that is placed in an isotropic scattering medium. The vulnerable structures act as completely opaque or semi-transparent obstacles that block the light 'emitted' by the target structure. This model produces ray bundles in the safe regions and 'shadows' in the unsafe regions. These ray bundles are similar to the widespread and thus easily comprehensible natural phenomenon usually referred to as '*god rays*' or '*crepuscular rays*' (e.g., see Figure 2). We have refined this basic metaphor to provide valuable information to a physician and have implemented our method as a complete accessibility visualization system. We present the following technical contributions in this work:

- We propose an algorithm for the evaluation of *all* access paths to a tumor with respect to their safety. It takes into account the potential risks extracted from all of the available volumetric datasets (Section 3.2). We show that our method is flexible and can be adapted for various uses without changing the core algorithm. However, in this paper, we mostly refer to the medical use because of the available datasets and the given evaluation possibilities.

- We propose an algorithm for computing the amount of available leeway in the *safe* areas and show how this information can be saved in a form suitable for visualization (Section 3.3).

- We show how the information regarding the safety of access paths and the amount of leeway can be presented to a physician to assist in decision-making. Our interactive visualization system combines 3D representation for a good overview of all access paths with widely used 2D slice views for millimeter-accurate planning (Section 3.4).

We evaluate the applicability of our method for clinicians using real and artificial datasets for various medical tasks. We also compare the paths extracted by our algorithms for 19 real interventions with actual paths chosen by a highly skilled physician in an unsupervised environment. The evaluation results show strong evidence that our method not only reflects the possible access path choices of an experienced doctor but also has a good chance for a high acceptance rate in clinical practice.

## 2 Previous Work

Preoperative planning. Whereas navigation systems for intraoperative assistance are quite common in neurosurgery [13], preoperative planning, besides the proper integration of multiple modalities into navigation systems, remains an open problem. For example, Brunenberg *et al.* [9] and Essert *et al.* [14] calculate safe paths for deep-brain stimulation, and Navkar *et al.* [25] and Shamir *et al.* [31] calculate them for general minimally invasive brain surgery. In contrast to our approach, all of these algorithms consider only a single point as a possible target or entrance position. For simpler surgery tasks, which sometimes require only one image modality, several active path safety evaluation systems exist: Villard *et al.* [37] optimize the needle position for ablating malignant liver tumors by minimizing the size of an ellipsoid, which models the necrosis zone, needed to cover a tumor plus a safety margin. The optimization process is constrained by a collision detection algorithm to avoid the vital organs and uses an 'insertion window' that is drawn by a radiologist on the scanned patient's skin. Altrogge *et al.* [1] propose a similar approach, but they predict the necrosis zone more accurately using finite element simulation. VanCamberg *et al.* [35] use FEM-based simulation of tissue and needle deformations to compute the best needle path for performing breast biopsies. The chosen path is constrained to be at a safe distance from blood vessels. Schumann *et al.* [30] generate a list of access paths using a set of 2D constraint maps. The paths are ranked for suitability using multiple criteria and empirically determined weighting factors. These paths are then displayed one-by-one in slices of the original CT volume. Whereas these approaches try to make a decision for a physician, using computation-based prediction, our work concentrates on using visualization to assist the planning of interventions, where current automatic approaches are not suitable.

(a) (b)

Fig. 2. The basic idea: crepuscular rays formed by the shape of the trees or by the frame of a window. The sunlight is scattered in the dusty air and thus an observer gets an impression of separate ray bundles. (Images taken at Watkin's Glenn, NY, by the authors (a) and inside Bayleaf Farmstead by 'There and back again', Antony Scott)

Intraoperative guidance. Another approach to assisting physicians is the provision of additional information during the intervention. Viard *et al.* [36] show how tracking of an inserted needle can be achieved in an MRI-based setup. Colchester *et al.* [11] use a localizer superimposed on a video stream for the same task. Hansen *et al.* [17] propose an approach that augments real scenes in an operating room with a distance-controlled illustrative visualization of risk structures using a projector. Chentanez [10] proposes a method for simulating deformable tissue and needles that can be used to guide a rigid or steerable needle to reach the target and avoid vulnerable structures. These strategies help in performing the intervention through better visualization and control of the current situation, but they do not guide the surgeon towards the most feasible access paths and cannot show alternative corridors.

Crepuscular rays. Our approach, using crepuscular rays to visualize abstract information for accessibility planning uses existing computer graphics research in a completely new way. Computer graphic solutions for rendering crepuscular rays were introduced in research by Max [21], who first computed these rays for photorealistic rendering, and by Nishita *et al.* [27], who invented the airlight integral to compute the effects of light scattering by air particles. Instead of computing volumetric light rays, volumetric shadows can also be computed, as demonstrated by Baran *et al.* [7]. The corresponding computer graphics research question originates in the computation of exact from-region visibility as researched by Nirenstein *et al.* [26]. Due to the high complexity of this problem, it is most often approached by sampling the region, as performed, for example, by Wonka *et al.* [39].

Isovists. In the field of architecture, the formalism of isovists describes a similar scenario. It was first introduced by Tandy [32] and is explained in detail by Davis and Benedikt [12]. A single isovist is the volume of space that is visible from a given point in space. This

mathematical formalism nicely describes situations similar to our visualization metaphor.

Anatomy rendering. 3D rendering of human anatomy is usually performed with direct-volume rendering (DVR), whereas vulnerable structures, such as vessels, are often rendered as opaque geometry [28, 16] to reduce the computational load. However, rendering systems that allow correct rendering of translucent objects and multiple intersecting volumes are attracting more attention due to advances in GPU processing power and flexibility. For example, Beyer *et al.* [8] use a multi-volume rendering system to build a brain surgery planning system. In this paper, we also use such a rendering system as proposed by Kainz *et al.* [19].

Access path visualization. Rieder *et al.* [28] visualize a possible access path by cutting out all tissue in a cylindrical volume between the target and entry points. Baegert *et al.* [5, 6] visualize safe access areas through the abdominal skin of a patient as holes in a fully opaque surface. The decision for making such holes is based on optimization of a set of candidate access paths with regard to multiple criteria. A similar technique is used by Villard *et al.* [37], where the 'insertion window' is visualized as cut-away skin. Brunenberg *et al.* [9] compute safe paths for a neurosurgery scenario and visualize them as opaque geometry on the brain surface in a 3D rendering that displays vulnerable structures only. A selected path can be further inspected using cutting planes orthogonal to the probe axis. Vaillant *et al.* [34] evaluate a cost function along straight paths between the outer brain boundary and a target point. The computed values are then mapped to a color scale of the rendered brain surface. Although all of these access-path visualization techniques are easy to interpret, it should be noted that they make it difficult to observe the full needle trajectory or the vulnerable structures within the body, or they lack context information.

## 3 Method

To illustrate our idea, we propose the following thought experiment. Imagine that a person needs to find and pull out a small object from a dark and dusty room with many obstacles in the way. A blind search for the best location from which to reach the object will be difficult and error-prone. However, if the object is a lamp that is switched on, then the beams of light that form in the dusty air will guide the searching person to the best path to retrieve the lamp. The best path will be easily identifiable: it is where the light beams both are strong (which signifies few obstacles in the way of the light) and cover a large area (which implies that there will be more space to operate in).

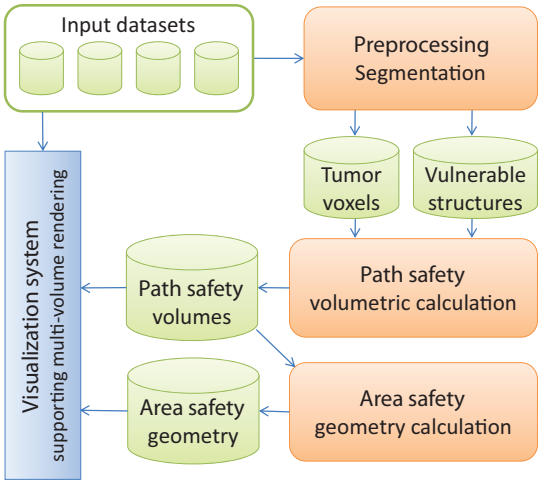


Fig. 3. The overview of the required steps for our visualization method.

In the following subsections, we describe how we employ this metaphor for the tumor-accessibility visualization task. The description will follow the basic data flow in our application, which is outlined in Figure 3. We will begin by describing how to define the target and blocking structures (the 'preprocessing' stage, Section 3.1). Then, we describe how the basic metaphor can be adapted to convey useful values to a physician and provide an algorithm for computing this information (the 'path safety' stage, Section 3.2). During the development of our method, we continuously consulted with clinicians to ensure that we would fulfill their needs. They drew our attention to the insufficiency of a simple projection of 3D data for 2D slice visualization. In section 3.3, we propose an algorithm for evaluating the extent of *safe* areas that is designed to solve this problem (the 'area safety' stage). Last, in section 3.4, we describe the visualization system that allows a physician to explore the data interactively.

### 3.1 Preprocessing

Preprocessing of the input datasets is necessary to classify the intensity values of the scanned volumetric datasets by their vulnerability. This type of classification is usually referred to as *segmentation*. This step depends heavily on the application and is described in detail for two examples in Appendix A, which can be found in supplemental material.

Often, a rough segmentation by thresholding the intensities to find impassable structures is sufficient. Thresholding can detect bone structures, which have very high intensity values in suitable imaging modalities (e.g., CT) or lungs, which usually have very low intensity values. However, this simple method is not applicable to distinguish more complex structures such as, for example, bronchial tubes, vessel trees, or neurological structures in the brain. Segmentation of these structures is an active area of research, and increasingly accurate algorithms are becoming available. Therefore, we have decided to leave the preprocessing as a completely independent and replaceable part of our method. In the subsequent steps, we can deal with all types of binary and continuous volumetric segmentation results.

Another application-dependent variable is the definition of the vulnerability of various structures. This definition must be made once by medical experts for each intervention type. Although a continuous scale for *vulnerability* would be easy to implement, our medical partners have suggested using a few discrete levels of vulnerability. Therefore, we use four to six levels for the examples in this paper, where low values denote non-vulnerable structures and high values denote impassable structures.

After the segmentation and classification of the relevant structures is completed, the safety margin may be added to the blocking information. The safety margin is necessary because of the inherent uncertainty that is caused by the change of relative organ position between the planning and actual intervention stages and the inherent uncertainty of segmentation methods. This change occurs due to respiration for abdominal interventions and due to brain shift, caused by the opening of the skull, for brain surgery. In our examples, we use a Gaussian smoothing filter with an empirically determined kernel size of 5 mm to add a smooth safety margin around all the blocking structures. The exact parameters of the safety margin can be determined by the end users for every type of application.

### 3.2 Path safety

We could use the light-scattering metaphor directly, but we want to convey to the user more valuable information than simply the amount of light reaching a certain point in space. Therefore, we generalize the light-scattering equation and search for a mathematical expression that maintains the basic 'beams of light' idea but also conveys information about dangerous structures on the way to the tumor. For convenience, we will use the light metaphor to describe the computed values in the rest of this section.

The amount of scattered light reaching a viewpoint from a direction $\mathbf{r}$ is obtained using the low-albedo volume rendering integral [23]:

$$I(\mathbf{r}) = \int_0^L I_s(s) \cdot e^{-\int_0^s \tau(t)\mathrm{d}t} \mathrm{d}s, \qquad (1)$$

where $L$ is the length of ray $\mathbf{r}$, $I_s$ is the intensity of light scattered by particles in the air in the direction of the viewpoint, and $\tau$ is the extinction coefficient.

The definition of $I_s$ depends on the value that is to be visualized and, in general, can be arbitrarily complex. However, for this paper, we define $I_s$ using two functions. The first function, which we call the *ray accumulation* function, governs the computation of the amount of light $I_p$ from a point source that reaches a certain point in space. To compute the light intensity reaching that point from the entire target structure, we represent the target structure as a union of an infinite number of point sources. The way that the intensities from different point sources are combined into the final intensity $I_s$ is described by the *ray combination* function. The definitions of ray accumulation and ray combination functions that we found useful in the case of medical interventions are described further (see Figure 4 for comparison) in the following.

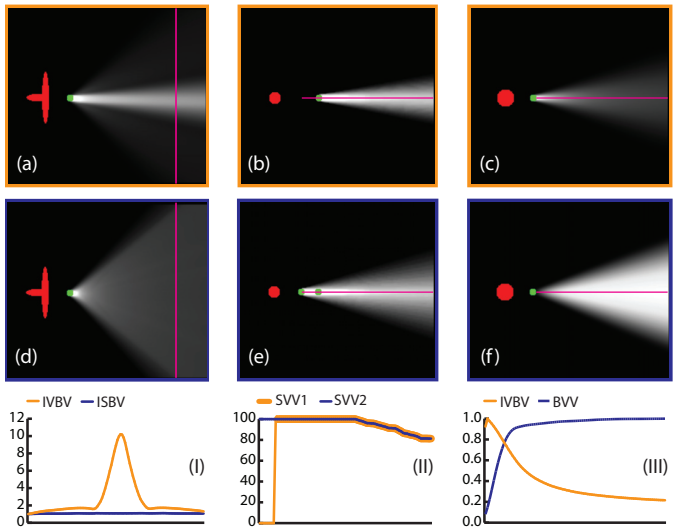


Fig. 4. Comparison of the behavior of various value-accumulation strategies. The images show the slices of the path safety volumes computed for different configurations of the target structure (shown in red) and blocking structures (shown in green). Panels (a) and (c) show the integral volume blocking value (IVBV); (b) and (e) show the surface visibility value (inverted, for better grayscale perception) with one (SVV1) and two (SVV2) blocking structures; (d) shows the integral surface blocking value (ISBV); and (f) shows the blocker volume value (BVV). The plots (I), (II) and (III) show the comparison of profiles along the lines in corresponding columns. The ordinate axis in the plots shows the ratio of the value to the minimum value along the entire line (I), the actual computed value (II) and the ratio of the value to the maximum value along the entire line (III).

The **surface visibility value** shows the percentage of the target structure surface facing a certain point that can be reached from that point without any significant blocking structures on the way:

$$I_p^{perc}(\mathbf{p}, \mathbf{x_0}) = \mathbf{I}_{[0,\epsilon)} \left( \int_C b(\mathbf{x}) \, \mathrm{d}s \right) \tag{2}$$

$$I_s^{perc}(\mathbf{x_1}) = \frac{\iint_{\partial\mathfrak{T}_+} I_p^{perc}(\mathbf{x}, \mathbf{x_1}) \, \mathrm{d}S}{A(\partial\mathfrak{T}_+)} \cdot 100\%, \tag{3}$$

where $C$ is a line segment from the point source $\mathbf{p}$ to a point in space $\mathbf{x_0}$, $b(\mathbf{x})$ is the blocking value function, $\mathfrak{T}$ is the target structure, $\mathbf{I}(x)$ is the indicator function, $\epsilon$ is the desired threshold for insignificant blocking values, and $A(\partial\mathfrak{T}_+)$ signifies the area of $\partial\mathfrak{T}_+$. Also, $\partial\mathfrak{T}_+$ is the part of the target structure's surface visible from the point $\mathbf{p}$, considering only self-occlusion of the target structure (see Figure 5):

$$\partial\mathfrak{T}_+ = \left\{ \mathbf{x} \in \partial\mathfrak{T} : \textstyle\int_C \mathbf{I}_{\mathfrak{T}}(\mathbf{p}) \mathrm{d}s = 0 \right\}. \tag{4}$$

We refer to it as the *front-facing* part of a surface. We also define the *back-facing* part of a surface, which we use further, as:

$$\partial\mathfrak{T}_- = \left\{ \mathbf{x}' \in \partial\mathfrak{T} : \textstyle\int_{C'} \mathbf{I}_{\mathfrak{T}}(\mathbf{p}) \mathrm{d}s = 0 \right\}, \tag{5}$$

where $C'$ is the ray starting at point $\mathbf{x}$ in the direction from $\mathbf{p}$ to $\mathbf{x}$.

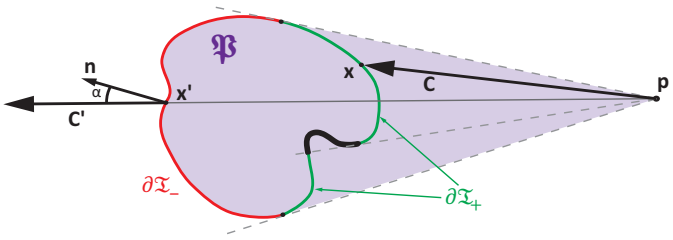


Fig. 5. Illustration of various structures used in our method: $\partial\mathfrak{T}_+$ is the front-facing and $\partial\mathfrak{T}_-$ is the back-facing part of the surface; $\mathbf{n}$ is a surface normal; and $\mathfrak{P}$ is the pyramid, with apex at point $\mathbf{p}$ and base $\partial\mathfrak{T}_-$

.

**Integral surface blocking value:** The surface visibility value, which is very easy to understand, is not able to distinguish cases where several blocking structures lie on the same ray to the tumor (see Figure 4(b, e, II)), which may lead to failure to provide information about safe paths in complex cases where the target structure is strongly occluded. To handle such cases, we propose functions that show the total weighted volume of blocking structures on the way from a point in space to the front-facing part of the target structure's surface:

$$I_p^{surf}(\mathbf{p}, \mathbf{x_0}) = \int_C b(\mathbf{x}) \, \mathrm{d}s \tag{6}$$

$$I_s^{surf}(\mathbf{x_1}) = \iint_{\partial\mathfrak{T}_+} I_p^{surf}(\mathbf{x}, \mathbf{x_1}) \, \mathrm{d}S, \tag{7}$$

**Integral volume blocking value.** In some cases, such as tumor surgery, the blocked *volume* of the target structure is of interest. The functions to compute this information are defined similarly to the integral surface blocking value:

$$I_s^{vol}(\mathbf{x_1}) = \iiint_{\mathfrak{T}} I_p^{vol}(\mathbf{x}, \mathbf{x_1}) \, \mathrm{d}V, \tag{8}$$

where function $I_p^{vol}$ is the same as in Eq. (6). Because we consider straight paths only, the integral volume blocking value can be also defined as:

$$I_p^{vol'}(\mathbf{p}, \mathbf{x_0}) = \int_C b(\mathbf{x}) \, \mathrm{d}s \cdot \int_C \mathbf{I}_{\mathfrak{T}}(\mathbf{x}) \, \mathrm{d}s \tag{9}$$

$$I_s^{vol'}(\mathbf{x_1}) = \iint_{\partial\mathfrak{T}_-} I_p^{vol'}(\mathbf{x}, \mathbf{x_1}) \, \mathrm{d}S. \tag{10}$$

Using this definition, the subsequent evaluation of these integrals is less computationally intensive.

The **blocker volume value** shows the total weighted volume of blocking structures on the way from a point in space to the entire target structure. It can be computed as a volume integral over the pyramid $\mathfrak{P}$, with the apex as the point and the base as the back-facing part of the target structure's surface (see Figure 5). After conversion from an integral in a spherical coordinate system, the blocker volume value can be defined as:

$$I_p^{block}(\mathbf{p}, \mathbf{x_0}) = \int_C b(\mathbf{x}) \cdot d^2(\mathbf{x}) \cdot \cos(\alpha) \, \mathrm{d}s \tag{11}$$

$$I_s^{block}(\mathbf{x_1}) = \iint_{\partial\mathfrak{T}_-} I_p^{block}(\mathbf{x}, \mathbf{x_1}) \, \mathrm{d}S, \tag{12}$$

where $\alpha$ is the angle between the normal to the surface at point $\mathbf{x_0}$ and the ray.

Discretization. We assume that the scattering is isotropic, and therefore the amount of light scattered at each point in space is viewpoint-independent. Consequently, we can precompute the values of $I_s$ in the region of interest in an offline step and store them as a volumetric dataset (in the rest of the paper, we refer to this volume as the *path safety volume*). This volume is then used by a multi-volume rendering system [19] to evaluate equation (1). We choose the region of interest to be a bounding sphere of all the vulnerable structures, centered at the centroid of the target structure. We use a regular grid to cover the target domain and set its spacing to the minimum of the spacings of the input datasets.

Then, for every voxel of the output volume, we cast rays through the blocking volumes to every voxel of the target area, which changes according to the function being computed. For each ray, we accumulate the value using a discretized ray accumulation function. Figure 6 illustrates this process. The sampling distance is chosen to be half of the smallest input volume spacing, which will automatically satisfy the Nyquist criterion for all the input volumes. The values accumulated for different rays are then combined with a discretized version of the ray accumulation function to produce the final value of $I_s$ that is stored in the path safety volume.

The discretization of all of the ray accumulation and ray combination functions is done in a similar way. For example, for the case of the blocker volume value, the discretized version of the ray accumulation function (Equation (11)) is:

$$I_p^{block} = \sum_{i=1}^{N_s} b_i \cdot V_{sample_i} \tag{13}$$

$$V_{sample_i} = s^2 |\cos(\alpha)| \frac{i^2}{N_s^2} l_{step}, \tag{14}$$

where $N_s$ is the number of samples along the ray, $b_i$ is the $i^{th}$ sampled blocking value, $s$ is the spacing of the target structure volume, $l_{step}$ is the length of a single step along the ray, and $\alpha$ is the angle between the normal to the surface and the ray direction. $V_{sample_i}$ is the volume of the $i^{th}$ sample (see Figure 6). Note that no blocking structures will be missed when casting the rays, because the Nyquist criterion is satisfied, and the maximum distance between cast rays does not exceed the spacing of the blocking volumes.

The discretized version of the ray combination function (Equation (12)) is defined as:

$$I_s^{surf} = \sum_{j=1}^{N_v} I_{p_j}, \tag{15}$$

where $N_v$ is the total number of rays cast from the voxel, and $I_{p_j}$ is the corresponding ray value.

### 3.3 Area safety

Many physicians often prefer using multi-planar reconstruction views instead of, or in combination with, a 3D view. To convey the safety information in 2D views, we display the relevant slices of the path safety volume. However, because the 2D slices lack depth information, it is difficult to determine the overall extent of a safe area (unlike 3D, where safe areas can be identified at a glance). To address this problem, we propose the following algorithm:

1. Approximate the target structure surface using a geometry.
2. Extrude each vertex of the geometry in the direction of its normal until a certain distance or an 'unsafe' point is reached.
3. Classify vertices as 'safe' and 'unsafe', and determine the connected regions containing only 'safe' vertices.
4. Weight each vertex based on the size of the connected safe cluster to which it belongs.

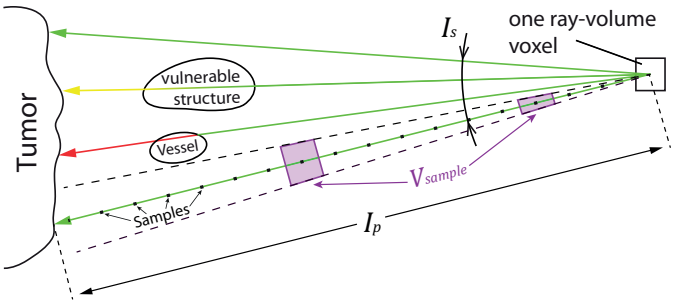


Fig. 6. Illustration of the calculation of the integral voxel value for one voxel. Impassable or very dangerous structures raise the accumulated 'ray value' $I_p$ quickly to high values. Other vulnerable structures gradually increase the accumulated value based on their size. Separate ray values are then combined to a voxel value $I_s$. $V_{sample}$ is the approximated volume of the sample, which increases with distance from the voxel. It is used to avoid weakening of the effect of dangerous structures with distance for the blocker volume value.

5. Display a corresponding slice of the computed geometry to provide additional information about the overall extent of the safe regions.

The criterion for considering a certain point in space to be 'unsafe' can be varied based on the application. Usually, a point is considered unsafe if the path safety at the point exceeds a certain threshold. However, we can also use the blocking value datasets to determine if the point is unsafe. In this way, the described algorithm can be used as a fast preview of the path safety. However, it cannot act as a replacement for the path safety computation method, as it takes only a few paths into account and cannot distinguish between medium-safe and dangerous paths.

We approximate the segmented tumor with an ellipsoid to avoid non-manifold faces and overlaps during the extrusion process. We align the ellipsoid's axes with three main axes of the tumor, which are extracted using principal component analysis of the tumor voxel coordinates. We tessellate the ellipsoid using a regular grid in a spherical coordinate system, i.e., the angular distances between the vertices of the ellipsoid are equal in both angular directions. The tessellation level is chosen in such a way that after extrusion the maximum edge length does not exceed the spacing of the output volume of the path safety calculation.

Every vertex of the ellipsoid is subsequently extruded in the direction of its normal vector until a certain distance or an unsafe point is reached. We choose normal direction in order to avoid nonmanifold and intersecting faces in the resulting geometry. We then separate the vertices of the resulting geometry into two classes: the 'safe' class, which contains the vertices that have been extruded up to the fixed distance, and the 'unsafe' class, which contains the vertices whose extrusion was stopped because the safety criterion was violated. Because of this binary separation, we can directly define disjoint connected safe regions. For each of these regions, we compute the mass and save it as a scalar property with every vertex belonging to the region. The algorithm for the mass calculation uses the discrete form of the divergence theorem with the general assumption that the surface is watertight, as described by Alyassin *et al.* [3]. In the rest of the paper, we refer to the resulting geometry with weighted vertices as the *area safety geometry*.

### 3.4 Visualization system

Our visualization system contains two significant parts that are designated for separate stages of the intervention planning procedure. The first part is intended to provide a comprehensive overview of the safety of available paths and uses a 3D representation. The second part is designed for millimeter-accurate planning of the intervention when the access area is usually already chosen and uses a 2D slice representation. We allow the physician to switch between these modes interactively or use them together in a single visualization, combining the

advantages inherent in both perspectives.

Path safety visualization. We use a multi-volume rendering system [19] to visualize the output of the path safety computation algorithm along with the original 3D body scans. Our rendering system also allows the addition of the segmentation results as translucent geometry if desired.

A simple one-dimensional transfer function is sufficient to control the visualization of the path safety volume. Depending on the value encoded into the path safety volume, the safe paths have either low values (in the case of integral volume or surface blocking value and blocker volume value) or high values (in the case of surface visibility value). We assign the green color to the very safe paths, yellow to the medium-safe paths, and red to extremely dangerous paths (the blue-to-yellow color scheme can be used for color-blind users, and our system also allows the definition of arbitrary color mappings). The user can remove certain safety classes from the visualization by setting their opacity value to zero to reduce the visual clutter. As the values in the path safety volume represent the intensity of 'emitted light' reaching a point in space, we do not perform additional lighting or shadowing during the ray casting of this volume. An example of the visualization of only the very safe and medium-safe paths can be seen in Figure 1(a).

Area safety visualization. For 2D visualization, we display slices of the available datasets using cutting planes with the desired orientations. The default layout uses axial, coronal, and sagittal orientations of the cutting planes, as these orientations are widespread in medicine. However, the user can choose an arbitrary orientation during the interaction. The 2D interaction scheme itself is similar to the one used in MITK [38].

The slices of the original datasets, segmented datasets, and path safety volume are displayed with a contour that results from the intersection of the cutting plane and the area safety geometry. We render this contour as an OpenGL triangle strip with varying thickness and color. For the color mapping of the available leeway, we use the same color scheme as for the three-dimensional path safety rendering. The thickness of the line segments is also defined by the area safety information. After discussion with our medical partners, we fixed the upper limit for the line thickness to be one centimeter in the patient coordinate system. Figure 1(b) shows a sample image of an axial slice of an artificial dataset rendered using our method.

**Algorithm 1 The path safety volume computation kernel in pseudo-code.** The sampling of the volumes is performed in the global coordinate system. $\Omega$ refers to a volume containing all information about the vulnerability of structures and $\Omega(p)$ to the volume sample at point $p$; $\mathfrak{T}$ defines a volume of tumor voxels and $\mathfrak{T}(p_t)$ the tumor voxel at point $p_t$; $I_{xyz}$ and $A_{xyz}$ are the virtual attenuated light intensities emitted by the tumor. $\Theta$ defines the output volume and $\Theta(p_o)$ the sample at position $p_o$. $\mathbf{M}_\Theta$ is the transform matrix from the local coordinate system of $\Theta$ to the global coordinate system. $\delta$ is the normalized direction of a virtual light ray scaled by the step size $\gamma$. The implementation of ACCUMULATEVALUE, COMBINEVALUES, and FINALIZEVALUE functions as well as the values of *initialIntensity* and *initialVoxelValue* depend on the value being computed (see Section 3.2).

```
1: function CASTRAY(p, δ, Ω, N_steps)
2:     A_xyz ← initialIntensity
3:     for N_steps do
4:         p ← p + δ                                   ▷ advance along ray
5:         A_xyz ← ACCUMULATEVALUE(A_xyz, Ω(p))
6:     end for
7:     return A_xyz
8: end function
9: function COMPUTEACCESSIBILITY(Ω,𝔗)
10:    setup computation grid
11:    for all GPU THREADS do   ▷ is done in parallel on the GPU
12:        p ← thread's index in the computation grid
13:        p ← M_Θ · (p · spacing(Θ))        ▷ get global coordinates
14:        if p ∉ sphere inscribed in Θ then
15:            return
16:        end if
17:        I_xyz ← initialVoxelValue
18:        γ ← 0.5 · min(spacing(Ω))                   ▷ Nyquist criterion
19:        for p_t ∈ 𝔗 do
20:            δ ← normalize(p_t − p) · γ ▷ calculate step direction
21:            I ← CASTRAY(p, δ, Ω, ⌈||p_t − p|| / γ⌉)
22:            I_xyz ← COMBINEVALUES(I_xyz, I)
23:        end for
24:        Θ(p) ← FINALIZEVALUE(I_xyz)
25:    end for
26: end function
```

## 4 IMPLEMENTATION

Precomputation. The path safety computation requires the evaluation of all possible and impossible access paths. This process is very computationally intensive, and a full evaluation might take up to several years using conventional CPU-based iterative approaches. Because the evaluation of the safety level of every voxel is completely decoupled from the evaluation for other voxels, our algorithm is very well suited for parallel computation. We implemented our path safety computation algorithm using NVidia's CUDA to utilize the available processing power of the GPUs. The lookup volumes, including vulnerable structures and impassable structures, are stored in the GPU memory in the available texture units, allowing us to use the advantages of hardware trilinear interpolation and texture caching. The CUDA kernel for the fast path safety volume computation is outlined in Algorithm 1. We use 3D thread blocks with a size of $8\times8\times8$, which results in 512 threads per block. Every thread block processes a $8 \times 8 \times 8$ block of voxels. This layout allows better thread coherency and less texture-cache misses as compared to 1D ($\sim 20\%$ slower) or 2D ($\sim 3\%$ slower) voxel blocks. Each thread computes the path safety for exactly one output voxel.

The area safety computation algorithm is not as computationally intensive. Therefore, for simplicity and clarity of the implementation, we use the Visualization Toolkit (VTK [29]) for geometry extrusion and clustering.

Rendering. We use the Medical Imaging Interaction Toolkit (MITK [38]) as the core medical visualization system. MITK provides all of the necessary basic functionality for the visualization of medical data. We use MITK's built-in OpenGL-based 2D slice view functionality (achieved through 3D texture mapping) to display the abdominal data from an arbitrary imaging modality, and the path safety volume. Additionally, for area safety visualization we project the geometry's normal vectors onto the desired cutting planes and use them together with information about the current cluster size to render thick lines as OpenGL quad-strips. Thus, the projected normal vectors define the direction of the quads, and the additionally stored information about the mass of an area defines their size and therefore the thickness of the lines. For 3D visualization, we have integrated the polyhedral CUDA-based rendering system proposed by Kainz *et al.* [19] as a separate view in the widget system provided by MITK.

Performance. Although the direct geometric area safety calculation is performed in a couple of seconds on the CPU ($O(n)$ complexity, where $n$ is the number of vertices in the mesh approximating the tumor), the path safety volume calculation depends strongly on the number of voxels in the segmented tumor ($O(n^3 \cdot m)$ complexity, where $n$ is number of voxels per dimension of the output volume, and $m$ is the number of tumor voxels). As the voxel values are computed independently, we are able to split the output path safety volume into several parts and utilize multiple GPUs simultaneously (tumor and vulnerable structures information is duplicated on each GPU). With this approach, the evaluation of path safety takes $600ms$ per tumor voxel and approximately five minutes for the whole tumor on our test system (Intel QuadCore 3.16 GHz, 12 GB RAM, NVidia Quadro6000

and GTX580) for $512^3$ input data sets and a tumor with an average diameter of 2 cm (508 target tumor voxels). Note that we do not need to update this volume during visualization and planning and that this computation must be performed only once per intervention.

The required time for preprocessing depends strongly on the desired application and the available segmentation algorithms. During our experiments, these steps took from a few seconds (clear structures, segmented by thresholding) up to several minutes, including user input (brain DTI, fMRI evaluation, and sophisticated vessel-segmentation algorithms).

Memory requirements. Our method requires only the resulting segmentation volumes as an input. Whereas a pure binary segmentation can be stored as a one-bit single-value scalar field that combines all segmentation results, segmentations that also include levels of vulnerability and smooth safety margins have to be stored with a bit-depth at least comparable to that of the input volumes. Nevertheless, intersecting vulnerabilities can also be summed up and subsequently saved in a single volume. Overall, the required additional memory is not more than that of the input volume with the highest resolution. For our examples, we stored the blocking volumes in a floating-point 3D texture. The biggest dataset we used (pig abdomen) amounted to 512MB. The memory requirements of the geometric representation of access areas are negligible compared to those of the path safety volume. Whereas the path safety volume might require several hundred megabytes of storage space, the area safety geometry occupies approximately 10 MB, even at a very high polyhedral resolution ($\sim 600.000$ faces).

## 5 Results

We evaluated our accessibility visualization approach in several discussions with radiology experts during the implementation process. Our algorithms were successively refined using this expert knowledge. The results of this refinement process are different value-accumulation strategies for the calculation of safe and unsafe paths as they are presented in Section 3.2.

Qualitative user study. To verify the suitability of the chosen path and area safety visualizations for the prospective users, we conducted an online user study among 31 medical doctors of whom 15 have fully completed our survey. Of those 15 participants, 13% of the participants have been female [2/15] and 86% – male [13/15], with 80% expert knowlege in radiology, 26% neurology, 26% surgery, and 20% computer science and visualization (multiple fields of expertise have been possible). Their professional experience was between five and ten years for 46% [7/15], and more than ten years for 20% [3/15].

We divided the survey into two parts. During the first part, we evaluated the overall acceptance of our method in 3D and 2D, based on an eight-value Likert scale. We chose eight values to avoid neutral answers, which can occur for odd numbered scales (scales without midpoints are not less reliable than those scales with them [2, 4]). Our method was presented as turns in the pitch and yaw directions for 3D visualizations and as a complete scroll through all available slices for 2D slice-based visualization. The results in Figure 8 show that the 2D methods were preferred by the participants in our survey. This result can be explained by the high number of participating radiologists who are specially trained to work with 2D slice visualizations. The most successful 3D visualization was the one showing only the safe paths in 3D. The addition of medium-safe paths and impassable paths decreased the acceptance by most participants. However, the wide range of results indicates that the information desired to be seen in 3D depends on personal preferences and should remain adjustable by the user, as is the case in our system. For 2D slice-based visualization, an augmentation with our proposed area safety visualization method and a combination with the projection of the path safety volume received the highest grades. The projection of the path safety volume onto 2D slices alone showed lower acceptance on average, but the acceptance also showed large variation, which provides evidence for significant differences in personal preferences. Therefore, we assume that an adjustable visualization is also the best choice for 2D views.

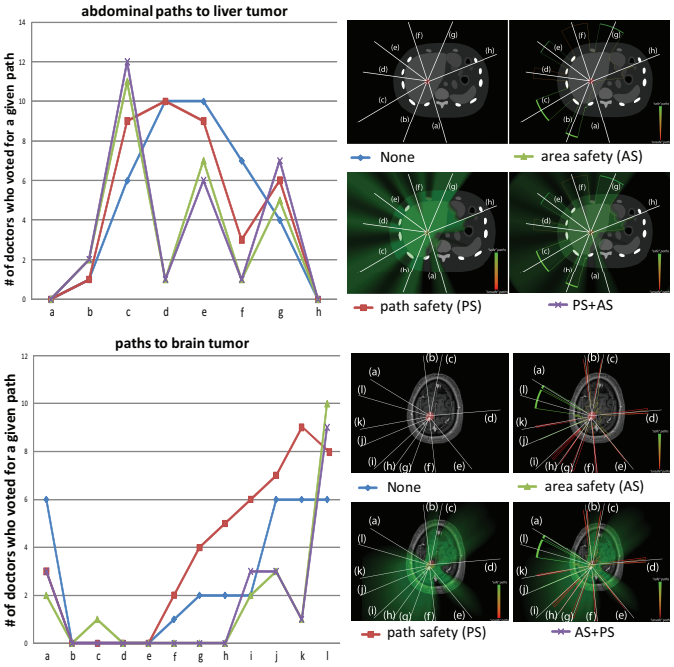


Fig. 7. Impact of our visualization method on path choice for generic cases. **PS** refers to the path safety volume calculation and its projection onto 2D slices. **AS** refers to the geometry augmentation in 2D including the visualization of the leeway (area safety). Note that our method has a strong influence on certain path decisions. For larger images please refer to supplemental material.

In the second part, we investigated the influence of our method on the choice of access paths for two cases: one liver and one brain tumor. We presented different options for access paths and observed how the decision changed with different accessibility visualizations. In the presented images, the green region shows the safest 20% of the paths, using blocker volume value as a measure. The questionnaire provided several choices for access paths, both feasible and dangerous, which were chosen in advance by a radiology expert and a neurology expert. We measured the number of feasible paths that were chosen by the participants. In the upper example in Figure 7, paths 'c,d,e' are the safest paths. For this example, the area safety calculation had the greatest impact. For example, path 'd' is safe but has very little leeway, which was shown with thin red lines by our algorithm. This factor motivated our survey participants to choose different paths when area safety information was shown in addition to the anatomical data. The same evidence can be seen in the lower graph of Figure 7, which shows an example of brain tumor surgery. Here, paths 'a,l,k' are the safest ones, but again, 'k' has very little leeway, which is visible in the area safety visualization. This factor influenced the participants' decision to avoid the path 'k'. Although no user chose a dangerous path using our methods, the tendency to choose a safe path increases when path safety and area safety are also displayed, as shown in Figure 7.

Overall, our method proved to be well-received by the participants in our survey. The results are summarized in Figure 8, which outlines the general expected acceptance in clinical practice, and in Figure 7, which shows the impact of our method on the expert decisions. Finally, we asked the participants if they would prefer a combination of the shown visualization methods. Most participants ($> 80$ %) would prefer a combination of a 3D volumetric representation, as shown in Figure 1(a), and a projection of the safe areas on 2D slices (both area safety and path safety information), as shown in Figure 1(b).

Gold standard comparison. In addition to the qualitative user study, which we performed to gain a subjective acceptance evaluation of the proposed accessibility-visualization method, we studied the accuracy of the displayed safety information, proposed by our algo-

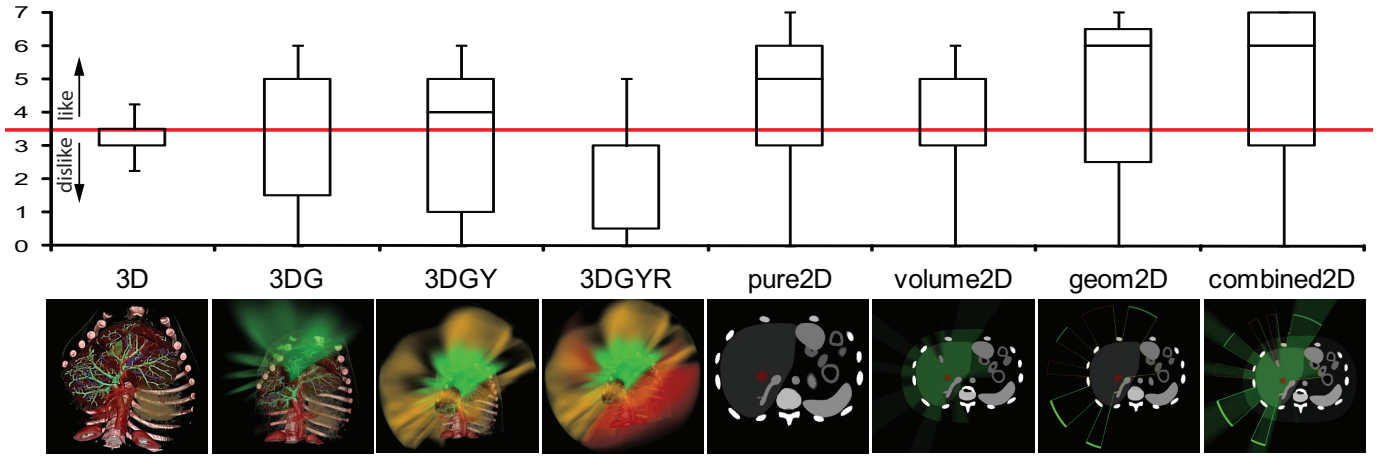


Fig. 8. Evaluation of the acceptance of our methods for clinical practice. The participants were offered a choice in the form of an eight-value Likert scale after watching a video of our method. The 2D methods were preferred and are indicated with *pure2D*. The acceptance of 3D methods decreased with increasing amounts of displayed information. The option labeled *3DG* shows safe paths only; *3DGY* also shows medium-safe paths; and *3DGYR* further adds impassable paths. 2D multi-planar methods were also evaluated with *area safety* geometry augmentation (*lines2D*), a 2D projection of the *path safety* volume (*volume2D*), and a combination of both (*combined2D*). For this box-plot, the ends of the whisker are set at $1.5\times$ interquartile range above the third quartile and $1.5\times$ interquartile range below the first quartile, which corresponds to the normal convention for box-plots. The thumbnails below each box show frames from the corresponding videos. For larger images please refer to supplemental material.

rithms, on 19 real abdominal CT-guided RFA interventions. To perform this study, we applied our visualization method to all available patient datasets and the vulnerable structures segmented from them. Subsequently, we compared the calculated path and area safety to the needle trajectory actually chosen for the intervention. This straight trajectory is available in a separate registered CT scan.

We considered the chosen paths as the gold standard because all of the performing physicians had more than 10 years of experience with minimally invasive abdominal interventions. Furthermore, all patients except one have not had complications after the intervention. The only case who suffered a complication (bleeding) also recovered after a short time. Several physicians who were consulted after the intervention were not able to find an explanation for this complication, which leads us to assume that the scan may have been of insufficient resolution to show all vulnerable structures for proper planning. We consider this case as valid for our study, because all rules to find an optimal access path were followed during the actual intervention. However, we excluded two cases from the study. The first case was excluded because the patient had an implanted medical pump and several aortic stents, and the intervention had to be specially adapted. The second case was not suitable for our study because the respiratory motion in the scan showing the needle trajectory was too strong for proper registration (this patient had several partial organ resections because of multiple cancer metastases). Hence, we used 90% of the valid example interventions for this retrospective gold standard study.

For 8 cases (47%), the needle trajectory coincided with a path for which our algorithm calculated a path safety of 100%, which means that in these cases, there were no obstacles on the way to the tumor along this path. In most of these cases, the access area with the largest leeway was chosen. We also discussed these patients with our medical partners, who confirmed that the position of the tumor was suited very well for minimally invasive intervention. The remaining cases can be considered to be difficult, and they had an average gold-standard path safety of 77% using our method.

To calculate the relative area safety of the chosen paths, we rate the areas in proportion to the largest available safe area (thus, the largest area has a safety of 100%). In 7 cases (41%), the experienced physician chose the access area with the largest leeway. The average area safety of the remaining 59% of cases was 70%, which shows clear evidence that areas with the most available leeway are always chosen by the experts and that our method reflects several decision criteria for real-world intervention planning.

## 6 Discussion and Future Work

Comparison to other approaches: For the sake of completeness, we compare the most advanced access path planning systems of Schumann *et al.* [30] and Baegert *et al.* [5] with our approach in Table 1. Note that the main difference is that our system aims to provide a visualization to assist in planning and leaves the freedom of decision to the performing physician instead of trying to find an optimal path in a fully automatic way.

Table 1. An overview of our accessibility evaluation system compared to the most similar systems proposed by Baegert *et al.* [5] and Schumann *et al.* [30]. The strengths of our method are highlighted with bold font.

| | **Baegert** | **Schumann** | **Ours** |
|---|---|---|---|
| **direct output** | one path | path list | **all paths** |
| **path visualization** | 3D[a] | 2D[b] | **3D+2D**[c] |
| **target structure** | point[d] | point[d] | **full tumor** |
| **computation space** | 2D | 2D | 3D |
| **computation time** | 30s[e] | 5s[f] | 30s – 300s[g] |
| **target application** | RFA | RFA | **generic** |
| **computation strategy** | two-pass | multi-pass | single-pass |
| **visualization strategy** | cut outs | one path | volumetric |

[a] areas and one path [b] one path [c] all paths [d] volumetric constraints
[e] depends on polygon resolution [f] depends on numerical constraints
[g] depends on tumor size

Area safety geometry computation: According to our user study, area safety geometry is a very good visual cue for understanding safety information in the 2D slice view. In future we plan to avoid the extrusion of the vertices in normal directions as some of the information stored in path safety volume might be missed. However, it should be noted that current geometry approximation is conservative (i.e. the geometric representation will not consider a point safe when the path safety volume states the opposite). One approach is to use a solid fitting algorithm [15] on the path safety volume to extract

the outer surface of the volume containing values in a safe interval of values.

Respiration compensation: During abdominal and thoracic interventions, the respiratory motion of the organs cannot be prevented, which poses a severe problem for applying offline planning results to the actual intervention. A feasible approach to deal with this problem is to apply our method to every stage of a patient-specific respiration simulation sequence, as is possible, for example, with the XCat patient model [20]. We can then apply fast GPU-based registration methods between the time steps and between the patient scan and the model (e.g., Optical Flow motion fields [33]) and hence integrate the patient-specific anatomy into the model. We can thus warp a single scan of a patient to enough discrete sampling points of a whole respiration cycle (usually 10-20) and apply our method to each of the resulting volumes. The resulting path safety volumes are combined in a volume that only classifies paths as *safe* if no vulnerable structures are hit in any of the respiration states.

Interventional augmented reality: In addition to planning an optimal access path, finding that path during the intervention itself is also a challenging task. Our visualization method can help in solving this task by integrating it into an augmented reality system. A photo of our prototype AR system can be found in supplemental material.

Other applications: The applications of our method are not limited to medicine. For example, it can be directly applied to mechanical accessibility assistance. An example visualization can be seen in Fig 10.

## 7 Conclusion

We effectively applied a natural metaphor to a difficult medical-accessibility decision problem. To exploit this metaphor, we calculate an additional volumetric dataset on the GPU, that encodes the safety of all possible access paths as bright rays shining out of the body, based on various replaceable segmentation procedures. Thus, the intensity values provide additional information on how much of the target structure can be reached from every position within the region of interest. Furthermore, we evaluate the available leeway for each ray bundle and display this information in 2D slices, which are widely used in medicine. With this method, a physician can quickly and reliably determine the possible tool trajectories. A combination of area and path safety augmented 2D MPR views was implemented in a medical visualization prototype, as shown in Figure 9. This figure also shows that our visualization approach can be easily used to indicate dangerous and impassable areas instead of safe areas only.

Study results. We performed three different evaluations of our method. The first and most obvious one considered expert knowledge during the implementation process. We worked closely with medical experts and discussed all results during the various stages with them. However, in approximately 50% of the cases, our experts did not agree on a single optimal path. This disagreement was one of the main reasons we chose to visualize safe *areas* instead of direct path proposals as a single line.

The online survey we conducted was mainly intended to evaluate the acceptance of the proposed visual enhancement by a broader medical audience. A full medical evaluation would also include a study on the intervention outcome of various medical procedures using our method compared to the classical planning approach based only on experience. Such a study is planned for our next project. The participants criticized the fact that the path selection took place in one selected axial plane only, although the plane was selected by an expert. In the future, we also plan to implement a scrollable medical-imaging interface for our online survey system.

Our retrospective gold-standard survey relies on the assumption of a perfect physician. As is shown by the available patient data, this assumption is of course not true. The treatment outcome depends strongly on the difficulties inherent to the tumor position and also on further circumstances such as the overall patient history. Therefore, this evaluation gives an impression of the possible prospective benefit for unskilled physicians, training simulators, and complication investigation.

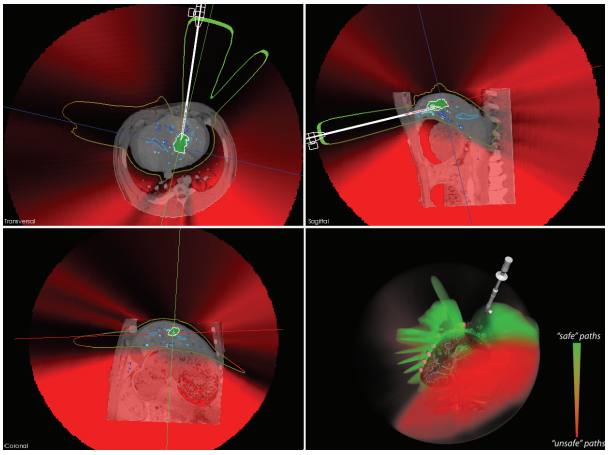


Fig. 9. A screenshot of our medical visualization system with *area safety* and *path safety* augmentation. In this example, the path safety volume shows all dangerous and impassable paths in red. The area safety geometry shows all safe access areas. The 2D MPR views are aligned with the direction of the main axis of one safe access area. For datasets similar to this one, which show mainly large safe access areas, the area safety geometry can be smoothed and additionally displayed as translucent geometry in 3D, as shown here. The tool to be placed into the tumor (green) is a RFA needle. All vulnerable vessels are displayed in shades of blue.

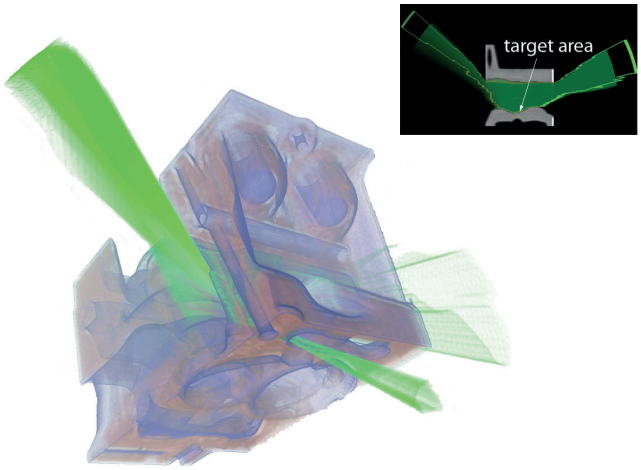


Fig. 10. An example of the applicability of our method to other fields of research. We have chosen a spot within an engine block that is difficult to reach. Because the engine block itself is solid, only 100% *'safe'* paths are displayed. All other paths are impassable. Note the non-obvious access path at the bottom of the image.

## Acknowledgments

We would like to thank Markus Hadwiger, Meister Eduard Gröller, Marc Streit, and Alex Lex for their valuable comments. Further we would like to thank Michael Moche and Daniel Seider from Medical University Leipzig and Horst Portugaller from Medical University Graz for enough datasets and valuable discussions. This work was funded by the European Union in FP7 VPH initiative under contract number 223877 (IMPPACT).

## REFERENCES


[1] I. Altrogge, T. Kröger, T. Preusser, C. Büskens, P. L. Pereira, D. Schmidt, A. Weihusen, and H. O. Peitgen. Towards optimization of probe placement for radio-frequency ablation. In *Medical Image Computing and Computer-Assisted Intervention (MICCAI)*, volume 4190 of *LNCS*, pages 486–493. Springer, 2006.

[2] D. F. Alwin and J. A. Krosnick. The Reliability of Survey Attitude Measurement. *Sociological Methods & Research*, 20(1):139–181, Aug. 1991.

[3] A. M. Alyassin, J. L. Lancaster, J. H. Downs, and P. T. Fox. Evaluation of new algorithms for the interactive measurement of surface area and volume. *Med. Phys.*, 6:741–52, 1994.

[4] F. M. Andrews. Construct validity and error components of survey measures: A structural modeling approach. *Public Opinion Quarterly*, 48(2):409–442, 1984.

[5] C. Baegert, C. Villard, P. Schreck, and L. Soler. Multi-criteria trajectory planning for hepatic radiofrequency ablation. In *Medical Image Computing and Computer-Assisted Intervention (MICCAI)*, volume 4792/200 of *LNCS*, pages 676–684, 2007.

[6] C. Baegert, C. Villard, P. Schreck, and L. Soler. Precise determination of regions of interest for hepatic RFA planning. In *SPIE Medical Imaging 2007: Visualization and Image-Guided Procedures*, volume 6509, pages 650923–650923–8, San Diego, CA, USA, 2007.

[7] I. Baran, J. Chen, J. Ragan-Kelley, F. Durand, and J. Lehtinen. A hierarchical volumetric shadow algorithm for single scattering. *ACM Trans. Graph.*, 29:178:1–178:10, December 2010.

[8] J. Beyer, M. Hadwiger, S. Wolfsberger, and K. Buhler. High-quality multimodal volume rendering for preoperative planning of neurosurgical interventions. *IEEE Trans. on Visualization and Computer Graphics*, 13:1696–1703, 2007.

[9] E. J. L. Brunenberg, A. Vilanova, V. Visser-Vandewalle, Y. Temel, L. Ackermans, B. Platel, and B. M. T. H. Romeny. Automatic trajectory planning for deep brain stimulation: a feasibility study. In *Medical Image Computing and Computer-Assisted Intervention (MICCAI)*, LNCS, pages 584–592. Springer, 2007.

[10] N. Chentanez, R. Alterovitz, D. Ritchie, L. Cho, K. K. Hauser, K. Goldberg, J. R. Shewchuk, and J. F. O'Brien. Interactive simulation of surgical needle insertion and steering. In *ACM Trans. Graph.*, page 88:188:10. ACM, 2009.

[11] A. C. Colchester, J. Zhao, K. S. Holton-Tainter, C. J. Henri, N. Maitland, P. T. Roberts, C. G. Harris, and R. J. Evans. Development and preliminary evaluation of VISLAN, a surgical planning and guidance system using intra-operative video imaging. *Med. Image Analysis*, 1(1):73–90, Mar. 1996.

[12] L. S. Davis and M. L. Benedikt. Computational models of space: Isovists and isovist fields. *Computer Graphics and Image Processing*, 11(1):49–72, Sept. 1979.

[13] S. DiMaio, N. Archip, N. Hata, I.-F. Talos, S. Warfield, A. Majumdar, N. Mcdannold, K. Hynynen, P. Morrison, W. W. III, D. Kacher, R. Ellis, A. Golby, P. Black, F. Jolesz, and R. Kikinis. Image-guided Neurosurgery at Brigham and Women's Hospital. 25(5):67–73, 09 2006.

[14] C. Essert, C. Haegelen, and P. Jannin. Automatic computation of electrodes trajectory for deep brain stimulation. In *Proceedings of the 5th international conference on Medical imaging and augmented reality*, MIAR'10, pages 149–158, Berlin, Heidelberg, 2010. Springer-Verlag.

[15] I. Fujishiro and Y. Takeshima. Solid fitting: Field interval analysis for effective volume exploration. In *Dagstuhl '97, Scientific Visualization*, pages 65–70, Washington, DC, USA, 1999. IEEE Computer Society.

[16] B. Geveci, U. Ayachit, J. Baumes, M. Bostock, V. Ogievetsky, B. Wylie, T. M. Shead, E. Santos, T. Ropinski, and J.-S. Praßni. DIY vis applications. In *Tutorial at the IEEE Visualization Conf.*, 2010.

[17] C. Hansen, J. Wieferich, F. Ritter, C. Rieder, and H.-O. Peitgen. Illustrative visualization of 3d planning models for augmented reality in liver surgery. *Int. Journal of Computer Assisted Radiology and Surgery*, 5:133–141, 2010.

[18] P. Hildebrand, T. Leibecke, M. Kleemann, L. Mirow, M. Birth, H. Bruch, and C. Burk. Influence of operator experience in radiofrequency ablation of malignant liver tumours on treatment outcome. *European Journal of Surgical Oncology*, 32(4):430–434, May 2006.

[19] B. Kainz, M. Grabner, A. Bornik, S. Hauswiesner, J. Muehl, and D. Schmalstieg. Ray casting of multiple volumetric datasets with polyhedral boundaries on manycore gpus. *ACM Trans. Graph.*, 28(5):Article No. 152, 2009.

[20] T. Marin, M. N. Wernick, Y. Yang, and J. G. Brankov. Motion-compensated reconstruction of gated cardiac spect images using a deformable mesh model. In *IEEE Int. Conf. on biomedical imaging: from nano to macro*, pages 520–523. IEEE Press, 2010.

[21] N. L. Max. Atmospheric illumination and shadows. In *ACM SIGGRAPH Computer Graphics*, pages 117–124. ACM, 1986.

[22] R. J. McDonald, L. A. Gray, H. J. Cloft, K. R. Thielen, and D. F. Kallmes. The Effect of Operator Variability and Experience in Vertebroplasty Outcomes. *Radiology*, 253(2):478–485, 2009.

[23] M. Meißner, J. Huang, D. Bartz, K. Mueller, and R. Crawfis. A practical evaluation of popular volume rendering algorithms. In *IEEE Symp. on Volume visualization*, pages 81–90. ACM, 2000.

[24] C. Mueller, J. M. Hodgson, M. Brutsche, H.-P. Bestehorn, S. Marsch, A. P. Perruchoud, H. Roskamm, and H. J. Buettner. Operator experience and long term outcome after percutaneous coronary intervention. *Can J Cardiol*, 19:1047–51, 2003.

[25] N. V. Navkar, N. V. Tsekos, J. R. Stafford, J. S. Weinberg, and Z. Deng. Visualization and planning of neurosurgical interventions with straight access. In *Proceedings of the First international conference on Information processing in computer-assisted interventions*, IPCAI'10, pages 1–11. Springer, 2010.

[26] S. Nirenstein, E. Blake, and J. Gain. Exact from-region visibility culling. In *Eurographics Workshop on Rendering*, EGRW, pages 191–202. Eurographics Association, 2002. ACM ID: 581921.

[27] T. Nishita, Y. Miyawaki, and E. Nakamae. A shading model for atmospheric scattering considering luminous intensity distribution of light sources. In *ACM SIGGRAPH Computer Graphics*, volume 21, pages 303–310. ACM, Aug. 1987.

[28] C. Rieder, F. Ritter, M. Raspe, and H.-O. Peitgen. Interactive visualization of multimodal volume data for neurosurgical tumor treatment. *Comput. Graph. Forum*, 27(3):1055–1062, 2008.

[29] W. Schroeder, K. Martin, and B. Lorensen. *The Visualization Toolkit, Third Edition*. Kitware Inc., 2007.

[30] C. Schumann, J. Bieberstein, C. Trumm, D. Schmidt, P. Bruners, M. Niethammer, R. T. Hoffmann, A. H. Mahnken, P. L. Pereira, and H.-O. Peitgen. Fast automatic path proposal computation for hepatic needle placement. volume 7625 of *Proceedings of the SPIE*, pages 76251J–1 – 76251J–10, 2010.

[31] R. R. Shamir, I. Tamir, E. Dabool, L. Joskowicz, and Y. Shoshan. A method for planning safe trajectories in image-guided keyhole neurosurgery. In *Proceedings of the 13th international conference on Medical image computing and computer-assisted intervention: Part III*, MICCAI'10, pages 457–464. Springer, 2010.

[32] C. R. V. Tandy and A. C. Murray. The Isovist Method of Landscape Survey. *Methods of Landscape Analysis*, pages 9–10, Oct. 1967.

[33] M. Urschler, M. Werlberger, E. Scheurer, and H. Bischof. Robust optical flow based deformable registration of thoracic ct images. In *MICCAI Workshop Medical Image Analysis in the Clinic: A Grand Challenge*, LNCS. Springer, September 2010.

[34] M. Vaillant, C. Davatzikos, R. Taylor, and R. Bryan. A path-planning algorithm for image-guided neurosurgery. In *Joint Conf. Computer Vision, Virtual Reality and Robotics in Medicine and Medical Robotics and Computer-Assisted Surgery*, volume 1205 of *LNCS*, pages 467–476. Springer, 1997.

[35] L. Vancamberg, A. Sahbani, S. Muller, and G. Morel. Needle path planning for digital breast tomosynthesis biopsy. In *Robotics and Automation (ICRA)*, pages 2062 –2067, May 2010.

[36] R. Viard, N. Betrouni, J. Rousseau, S. Mordon, O. Ernst, and S. Maouche. Needle positioning in interventional mri procedure: real time optical localisation and accordance with the roadmap. In *Engineering in Medicine and Biology Society (EMBS)*, pages 2748–2751, Aug. 2007.

[37] C. Villard, L. Soler, and A. Gangi. Radiofrequency ablation of hepatic tumors: simulation, planning, and contribution of virtual reality and haptics. *Comput. Methods Biomech Biomed. Engin.*, 8(4):215–227, Aug. 2005.

[38] I. Wolf, M. Vetter, I. Wegner, T. Böttger, M. Nolden, M. Schöbinger, M. Hastenteufel, T. Kunert, and H.-P. Meinzer. The medical imaging interaction toolkit. *Medical Image Analysis*, 9(6):594 – 604, 2005. ITK - Open science - combining open data and open source software: Medical image analysis with the Insight Toolkit.

[39] P. Wonka, M. Wimmer, K. Zhou, S. Maierhofer, G. Hesina, and A. Reshetov. Guided visibility sampling. In *ACM Transactions on Graphics*, volume 25, pages 494–502. ACM, July 2006.